Four-Dimensional Studies of Morphology Evolution in Lithium−Sulfur Batteries

Chun Tan,[†] Thomas M. M. Heenan,[†] Ralf F. Ziesche,[†] Sohrab R. Daemi,[†] Jennifer Hack,[†] Maximilian Maier,[†] Shashidhara Marathe,[‡] Christoph Rau,[‡] Daniel J. L. Brett,[†] and Paul R. Shearing[*,†]

[†]Electrochemical Innovation Lab, Department of Chemical Engineering, University College London, Torrington Place, London WC1E 7JE, United Kingdom

[‡]Diamond Light Source Ltd, Harwell Science & Innovation Campus, Didcot, Oxfordshire OX11 0DE, United Kingdom

S *Supporting Information*

ABSTRACT: Lithium sulfur (Li−S) batteries have great potential as a successor to Li-ion batteries, but their commercialization has been complicated by a multitude of issues stemming from their complex multiphase chemistry. In situ X-ray tomography investigations enable direct observations to be made about a battery, providing unprecedented insight into the microstructural evolution of the sulfur cathode and shedding light on the reaction kinetics of the sulfur phase. Here, for the first time, the morphology of a sulfur cathode was visualized in 3D as a function of state of charge at high temporal and spatial resolution. While elemental sulfur was originally well-dispersed throughout the uncycled cathode, subsequent charging resulted in the formation of sulfur clusters along preferred orthogonal orientations in the cathode. The electrical conductivity of the cathode was found not to be rate-limiting, suggesting the need to optimize the loading of conductive carbon additives. The carbon and binder domain and surrounding bulk pore phase were visualized in the in situ cell, and contrast changes within both phases were successfully extracted. The applications of this technique are not limited to microstructural and morphological characterization, and the volumetric data can serve as a valuable input for true 3D computational modeling of Li−S batteries.

KEYWORDS: lithium sulfur, X-ray tomography, batteries, porous media, in situ characterization, synchrotron radiation
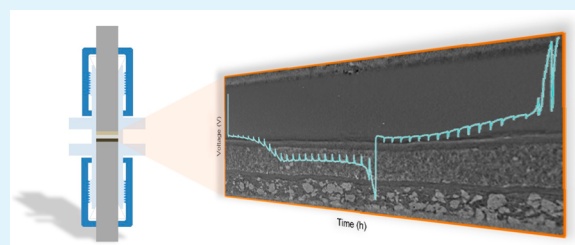
INTRODUCTION

Lithium sulfur (Li−S) batteries have the potential to supersede conventional Li-ion technology, particularly in applications that require high gravimetric energy densities, offering a factor of ca. 6 higher theoretical gravimetric energy density (2567 Wh kg^{-1} of sulfur) compared to Li-ion technology[1] (387 Wh kg^{-1} of LiCoO$_2$). However, despite further advantages such as the natural abundance and nontoxicity of sulfur, the commercialization of Li−S batteries has been complicated by poor cycle life and low Coulombic efficiencies.[2] These complications stem from the solubility in most organic liquid electrolytes of the intermediate polysulfide species formed during the conversion of S$_8$ to Li$_2$S during discharge and vice versa during charge. In addition to active material loss to the electrolyte phase, polysulfide solubility invariably results in a phenomenon known as the polysulfide shuttle effect, where mobile charged polysulfide species shuttle between the sulfur electrode and lithium metal electrode, driven by a potential difference and exacerbated at low C-rate. In addition to parasitic losses during charge, gas evolution results from degradation of the lithium metal anode because of side reactions with commonly used ether-based electrolytes.[3] Furthermore, a significant volumetric penalty on energy density arises from the need for a substantial amount of conductive carbon additives within the sulfur electrode because of the electrically insulating nature of S$_8$ and Li$_2$S.

Many approaches have been proposed in the literature to limit the adverse effects of polysulfide dissolution, including physical[4] or chemical polysulfide confinement, electrolyte optimization and solid state electrolytes, and surface protection of the lithium metal anode.[5,6] However, much has to be done to bridge the gap between fundamental materials research and optimization at the electrode and cell level.

Advanced characterization techniques applied to Li-ion batteries have seen growing interest in the Li−S community, with the goal of accelerating the development of new materials and optimizing electrode design and fabrication.[7] X-ray-based methods have become prominent in attempts to elucidate the complex mechanisms underpinning Li−S electrochemistry and to investigate the phenomenological origins of degradation within Li−S batteries.[8] The high brilliance of synchrotron sources has opened possibilities into in situ and operando examination of functional cells, allowing highly dynamic processes to be captured. In particular, the high temporal
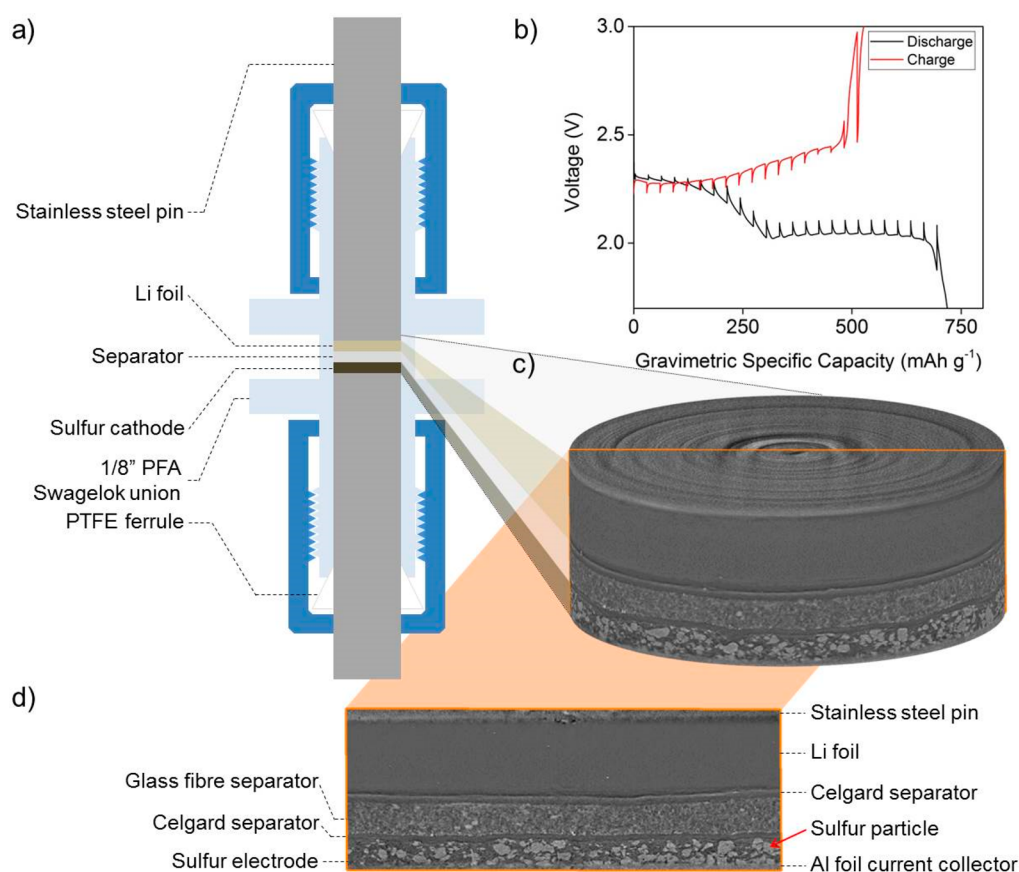
Figure 1. (a) Schematic of tomography cell (not to scale) with (b) electrochemical data for the first cycle, (c) volume rendering of a cropped region of interest within the uncycled cell, and (d) virtual slice of tomogram showing layers within the cell. Scale bar for the volume rendering and virtual slice represents 200 μm.

resolution achievable with X-ray diffraction (XRD)[9−11] and transmission X-ray microscopy (TXM)[11−13] has been harnessed by several authors to improve the mechanistic understanding of the phenomena occurring within a Li−S cell. Nelson et al. made the first foray into the use of TXM and XRD for the operando characterization of a Li−S pouch cell.[14] This was closely followed by in situ and operando XRD studies by Cañas et al.,[9] Waluś et al.,[10] and Kulisch et al.[15] Despite the high temporal resolution afforded by XRD and TXM, the main drawback of 2D techniques lies in the loss of depth information perpendicular to the plane of imaging. This may be evident in the conflicting observations made by all three groups regarding the formation of Li$_2$S during discharge: while Nelson et al. suggested that no Li$_2$S was formed at the end of discharge,[14] Waluś et al. detected Li$_2$S formation early during the low voltage discharge plateau,[10] whereas Cañas et al. found that Li$_2$S was only formed much later at 60% state of discharge.[9]

In common with all heterogeneous porous media, battery electrodes exhibit some degree of anisotropy, and the loss of spatial dimensions has significant implications when attempting to draw conclusions because of local variations in experimental measurements; for instance, variations in local current density, voltage, and consequently, local state of charge (SoC) cannot be excluded. However, despite the obvious advantages of 3D information, the temporal resolution achievable with tomographic techniques is often ca. 3 orders of magnitude slower (compared with 2D techniques) because

of the need to obtain sufficient angular projections for reconstruction. Therefore, initial applications of X-ray micro-CT were focused on postmortem degradation studies: Zielke et al. harvested electrodes from Li−S cells taken to different cycle numbers,[16] while Yu et al. pursued a hybrid approach of operando XRD and TXM investigations of a Li−S coin cell combined with ex situ X-ray micro-CT of harvested electrodes.[11] More recently, Sun et al. investigated lithium metal degradation within lithium polysulfide cells consisting of a monolithic carbon structure soaked with Li$_2$S$_8$ as catholyte. Six cells were each cycled to different cycle numbers and imaged with X-ray phase contrast tomography without disassembly.[17]

While postmortem characterization allows generalized conclusions to be drawn about degradation pathways, direct comparison is impossible between samples harvested from different cells, and cell disassembly may introduce uncertainty in the chemical state of the battery.[18] Furthermore, mechanistic investigations into the reaction processes occurring within Li−S cells require an in situ environment to consider solid to liquid phase transitions and a finer temporal resolution because of their highly transient nature. Of particular interest are "4D" (three spatial dimensions plus time) investigations performed under in situ or operando conditions.[19] This approach enables direct observations to be made about the same sample volume as a function of a time-dependent variable (these include state of charge, cycle life, or thermal cycling), eliminating uncertainty arising from the perturbation of and variability between samples.

The authors were among the first to perform in situ X-ray micro-CT on a functioning Li−S cell,[20,21] tracking micro-structural evolution within the same volume of a sulfur electrode as a function of cycle life. True operando microtomography of Li−S cells as a function of state of charge has remained elusive to date because of the reasons discussed earlier. In an operando absorption micro-CT and spatially resolved XRD study by Tonin et al., an acquisition time of ca. 20 min was reported while cycling a Li−S cell at an effective C/8 rate. Thickness changes within the Li metal anode were measured, along with observations on sulfur distribution and phase changes across two cycles, revealing severe Li anode degradation within the first cycle and migration of sulfur into the nonwoven carbon current collector.[22] However, shifts in electrode microstructure may be significant because of the substantial (ca. 4.2%) difference in SoC between the beginning and end of each measurement.

In this work, the operation of a Li−S battery was imaged in situ as a function of SoC at submicron resolution by synchrotron X-ray phase contrast micro-CT. To obtain a true representation of the state of the electrode, electro-chemical cycling of the cell was interrupted, which ensured a constant SoC during tomographic acquisition. For the first time to the authors' knowledge, the microstructure of a sulfur electrode was directly visualized in situ as a function of SoC with the aid of X-ray phase contrast, enabling the full identification and quantification of sulfur particles, carbon binder domain, and the electrolyte-filled bulk pore phase. Features such as the intrinsic porosity of the carbon binder domain (CBD) and Li_2S nanocrystals remain below the spatial resolution of the tomograms and are thus not directly segmentable. However, contrast values of the CBD and electrolyte phase were found to evolve as a function of state of charge, allowing for the indirect quantification of density changes arising from polysulfide dissolution and Li_2S formation.

This work demonstrates the full spatial and temporal resolution capabilities of synchrotron X-ray micro-CT, allowing morphological changes to be analyzed in situ with unprecedented detail as a function of state of charge. The benefits of this 4D approach extend beyond improving the mechanistic understanding of emerging battery technologies such as Li−S chemistry, to the wider field of heterogeneous porous media and the influence of microstructure on their performance and durability.

RESULTS AND DISCUSSION

A Li−S cell consisting of an elemental sulfur cathode and Li metal anode was built in a specialized electrochemical tomography cell adapted from a PFA Swagelok union described in our earlier work[20] and illustrated in Figure 1a. The cell was discharged and charged over one full cycle at an effective C/5 rate based on the initial discharge capacity of the sulfur electrode, equivalent to a C/12 rate based on the theoretical capacity of sulfur, with discharge interrupted during tomographic acquisition. Morphological parameters of the sulfur phase were extracted from volumetric image data at different states of charge through the first cycle, and where elemental sulfur was not present, contrast evolution of the carbon binder domain and surrounding electrolyte percolated bulk pore phase was analyzed.

Cycling of Tomography Cell. The tomography cell, presented in Figure 1 with associated first cycle electro-

chemical data and volume rendering of the uncycled cell, exhibited electrochemical performance that was in agreement with the literature for a similar electrolyte.[23] Electrochemical performance was also equivalent to larger 1/2″ Swagelok-type cells made from the same electrode material and electrolyte, demonstrating that the miniaturized cell design was sufficiently representative and that X-ray exposure had a negligible effect on the sample.[24] From Figure 1b, two characteristic discharge plateaus can be seen at ca. 2.2 V and ca. 2.0 V, and the cell achieved an initial discharge capacity of ca. 718 mAh g^{-1} and a reversible capacity of ca. 527 mAh g^{-1} for the initial charge based on the initial mass of sulfur. In subsequent sections, depth of discharge (DoD) and depth of charge (DoC) will be normalized to these capacities, respectively. Although comparable with the literature and larger format cells as discussed earlier, the low initial discharge capacity may be explained by the high mass loading of sulfur and, consequently, relatively low electrolyte-to-sulfur (E/S) ratio as outlined in the Methods section. Polyolefin separators were used on both lithium metal and cathode interfaces in order to achieve adequate spatial separation for image analysis. A third glass fiber separator was inserted in between the polyolefin separators to mitigate the low E/S ratio by acting as an electrolyte reservoir.

The ring artifacts seen in the stainless steel plunger in Figure 1c were due to sample tilt introducing variations in the center of rotation of the sample between the top and bottom of the detector. To reduce these artifacts within the region of interest (i.e., the electrode), a slice in the middle of the sulfur cathode was used to determine the center of rotation.

To visualize the microstructural and morphological changes of the sulfur electrode within the first cycle, the same virtual slice through the cathode is presented in Figure 2 as a function of state of charge. Each virtual slice is oriented with the current collector at the base, and five phases, namely, sulfur, Al current collector, carbon binder domain, separator, and the electrolyte-
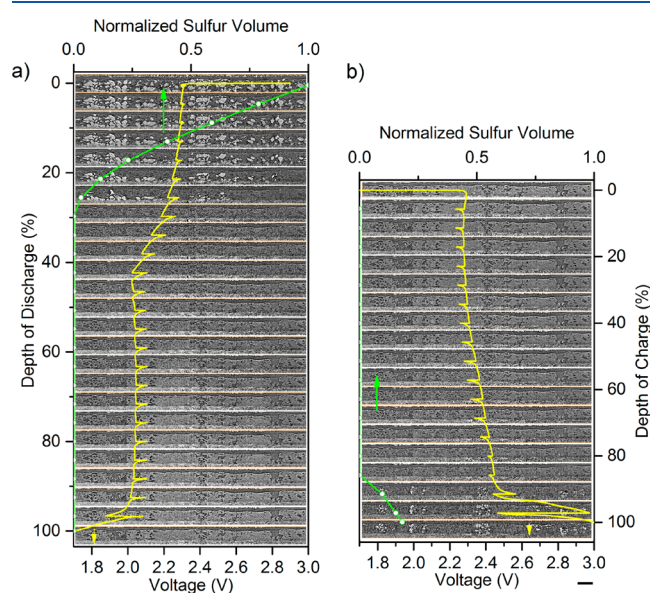

Figure 2. Reconstructed slices from (a) 100 to 0% DoD (based on initial discharge capacity of 718.2 mAh g^{-1}) and (b) 0 to 100% DoC (based on initial charge capacity of 526.7 mAh g^{-1}), with capacity−voltage and sulfur volume fraction curves (normalized to original volume of sulfur) overlaid in yellow and green, respectively. Scale bar represents 100 μm.
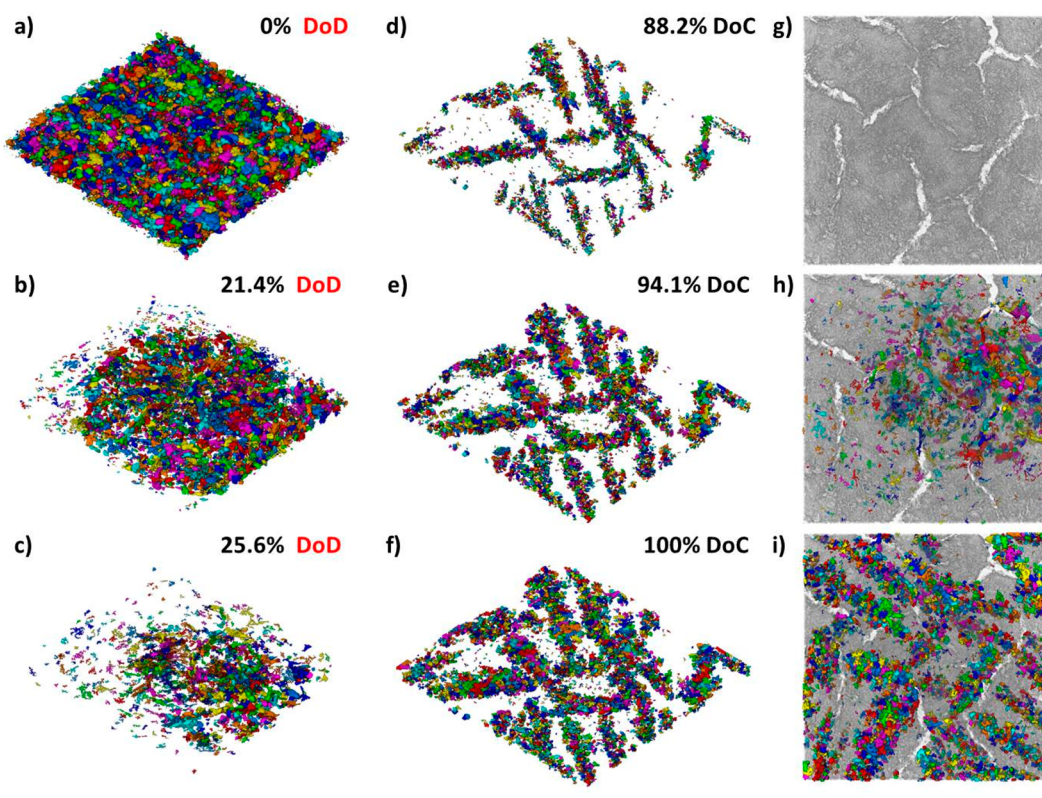
Figure 3. Volume renderings of individually labeled sulfur particles during (a−c) discharge and (d−f) charge. (g) Volume rendering of the CBD phase, showing (h) sulfur particles at 25.6% DoD and (i) 100% DoC. Scale bar represents 200 μm for all images.

filled bulk pore phase are visually distinguishable in descending order of brightness. State of charge and sulfur volume fraction curves (yellow and green lines respectively) are directly superimposed on the virtual slices in Figure 2, with each discontinuity on the yellow line and point on the green line corresponding to the tomogram acquired at that specific SoC.

Elemental sulfur was observed to completely disappear from the cathode within the first 30% of discharge as shown in Figure 2a, corresponding to ca. 213 mAh g^{-1} of capacity, suggesting the full conversion of solid elemental S$_8$ to soluble intermediate polysulfide species. From Figure 2b, macroscopic elemental sulfur particles were observed to reappear toward the end of charge at around 85% DoC. Specifically, in agreement with Kulisch et al.,[15] and a wider review of XRD investigations in the literature by Wild et al.,[25] sulfur was fully dissolved within the first half of the higher voltage plateau, which corresponds to the following reaction

$$2\text{Li} + \text{S}_8 \rightarrow \text{Li}_2\text{S}_8 \qquad (1)$$
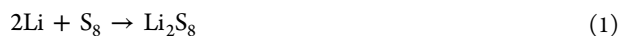
Although XRD is a powerful technique for phase *identification* of crystalline materials, there is limited scope for definitive phase *quantification* because of the 1D nature of the technique, where inferences have to be made from the intensities of the characteristic diffraction peaks. On the other hand, the spatially resolved density map generated by micro-CT enables direct quantification of sulfur particles, providing some insight into the reaction kinetics of the high voltage plateau. For a constant current discharge, the rate of sulfur dissolution is directly proportional to the slope of the sulfur volume fraction curve presented in Figure 2 (green line). An almost linear rate of dissolution was observed during discharge, in contrast to the seemingly limiting mass loading of sulfur

reached during the end of charge, and possible causes for this will be explored in a later section.

During the penultimate charge step, charging was interrupted close to the cutoff voltage of 3 V as the fixed 15 min charging interval had elapsed. A large overpotential of ca. 0.6 V was measured when the cell was relaxed, and there was some further growth of elemental sulfur particles in the final charge step. Two competing effects may account for this large overpotential, sulfur formation and an exacerbation of the polysulfide shuttle effect at higher voltages toward the end of charge.

Evolution of Elemental Sulfur Phase as a Function of State of Charge. Sulfur particles were individually labeled for size distribution analysis, and their volume renderings are presented in Figure 3 with the current collector below (not shown). As observable in Figure 3a−c, there was a radial variation in sulfur dissolution during discharge, with preferential dissolution from the circumference of the electrode inward. These variations may be an artifact of the diminutive form factor of the cell resulting in an electrode aspect ratio (thickness of the electrode compared to its width) where edge diffusion effects may be more apparent. Unfortunately, a trade-off is necessary between sample size and spatial resolution, especially when imaging at submicron resolution. Therefore, a radial correction factor (further details can be found in the Methods section and Supporting Information) was used to account for the dissolution front, and from this, the areal sulfur loading across the entire electrode was derived.

During charge, elemental sulfur crystals were found to grow in preferred orientations as shown in Figure 3d−f, originating from the center of the electrode disc. The presence of mud-crack patterns within the CBD shown in Figure 3g may have

increased the likelihood of sulfur nucleating around the ridges of the CBD bordering the cracks during charge, as evident in Figure 3i. The clustering of sulfur particles around the bulk pores formed during the drying of the electrode demonstrates the spatial influence that CBD morphology has during charge, underlining the need for spatially resolved studies. In addition to the entirely different morphology of sulfur formed, there was no radial variation of sulfur loading after charge, confirming suggestions by Wild et al. that the mechanisms behind charge are not the direct reversal of the discharge process.[25]

Sulfur Dissolution and Size Distribution Analysis. The actual sulfur mass loading of the whole electrode was quantified by applying a radial correction factor as discussed earlier, and these values are presented in Table 1 along with

Table 1. Morphological Parameters of the Sulfur Electrode during Discharge and Charge[a]

depth of discharge/ charge (%)	sulfur mass loading (mg cm^{-2})	theoretical number of electrons transferred from sulfur dissolution/(formation) (C cm^{-2})
Discharge		
0.0	6.20	–
4.7	4.89	0.495
8.9	3.66	0.463
13.0	2.47	0.446
17.2	1.42	0.398
21.4	0.71	0.265
25.6	0.20	0.194
Charge		
88.2	0.60	–
94.1	0.96	(0.135)
100.0	1.13	(0.064)

[a]Coulombs transferred from and to the sulfur electrode during each 15 min discharge or charge interval was ca. 0.671 C cm^{-2}.

state of charge information. Initial changes in sulfur mass loading during discharge largely stem from the electrochemical reactions occurring within the high voltage plateau, as elemental sulfur is not highly soluble in the binary 1,3-dioxolane/1,2-dimethoxyethane (DOL/DME) solvent used in this work. The reactions taking place at this plateau may therefore be decoupled, since the theoretical number of electrons consumed at the sulfur electrode resulting from the reaction in eq 1 is calculable directly from the change in sulfur mass loading, as shown in Table 1. While in each discharge interval, there was ca. 0.671 C cm^{-2} of electrons transferred to the sulfur electrode, the theoretical number of electrons that would be required for the amount of elemental sulfur disappearing in the same interval only accounts for a proportion of this, decreasing from ca. 0.495 to 0.194 C cm^{-2} as discharge progresses. This indicates that the reduction of S_8^{2-} to S_6^{2-} may be a result of both electrochemical and disproportionation reactions and not solely a result of the latter as suggested in the literature.[26] Furthermore, the complete disappearance of sulfur even with the comparatively high ca. 6.2 mg cm^{-2} sulfur mass loading of the electrode used in this work suggests that elemental sulfur utilization may not be a significant factor influencing capacity at relatively low C-rates. However, it must be acknowledged that the kinetics and mechanisms behind the multistep reactions within the Li−S battery are dependent on a multitude of factors including electrolyte choice and cell temperature.[25,27]

During charge, only a small proportion of electrons theoretically transferred from the sulfur electrode, ca. 0.135 out of 0.671 C cm^{-2}, results in the formation of elemental sulfur. There are a number of possible scenarios that may account for the difference in this areal charge density: parasitic losses stemming from the shuttle effect, the formation of nanosized sulfur particles (which fall below the resolution limit of this technique and are therefore not accounted for), or the ongoing conversion of polysulfide species (coincident with the formation of elemental sulfur) even close to the end of charge—the latter is consistent with the observed increase in electrolyte density at the end of charge as monitored by changing grayscale in the contrast analysis performed below. As discussed earlier, the growth of sulfur seemingly reaches a limiting mass loading, and this may be due to two opposing forces that influence the resulting mass loading on a fully charged cathode: while a higher C-rate may be beneficial in reducing the shuttle effect, increased polarization of the cell would result in premature termination of charging, limiting the achievable mass loading on charge. Conversely, a C-rate that is too low may result in an infinitely long charge because of the shuttle effect or hasten the depletion of the lithium nitrate additive used to suppress the shuttle effect.

Only tomograms at the beginning of discharge and end of charge, as presented in Figure 2, were found to contain visible elemental sulfur particles. These tomograms were binarized into sulfur and nonsulfur phases for the quantification of elemental sulfur within the cathode. Phase fractions of the sulfur particles in each cross-sectional slice of the electrode were calculated and shown as a function of normalized electrode thickness in Figure 4a, where 0 and 1 represents fixed positions within the separator and bulk sulfur electrode, respectively. The bulk electrode begins at ca. 0.45 of the normalized thickness in Figure 4a, because the nonuniform thickness of the uncalendered electrode results in a gradual tapering in sulfur phase fraction toward the separator. Sulfur is initially well-distributed within the electrode bulk, and as discharge begins, sulfur dissolution takes place throughout the electrode. The preferential dissolution of sulfur close to the electrode−separator interface suggests that the discharge of the cell is diffusion-limited at the beginning of the high voltage plateau. As the reaction front progresses into the electrode, a drastic increase in the porosity of the electrode is to be expected, as space initially occupied by the solid sulfur particles becomes pore space as the sulfur dissolves, and more electrode surface area for the reduction of polysulfide species is exposed.

Upon charge, preferential recrystallization of elemental sulfur occurs from the electrode−separator interface, indicating that the diffusion of higher order polysulfide species, rather than electrical conductivity within the CBD, is rate-limiting, since the electrical potential field of the electrode would theoretically be highest at the current collector. As discussed earlier, the preferential nucleation of sulfur around the CBD adjacent to the bulk pores of the electrode demonstrates the influence of inhomogeneities in porosity and tortuosity during charge. From these nucleation points, elemental sulfur then grows into the porous CBD as charge progresses, suggesting the involvement of electron transfer and implying that the final reaction step of solid sulfur formation is therefore electrochemical in nature.

Particle size distributions (PSDs) of sulfur particles from the electrode are presented in Figure 4c along with shape factor distributions in Figure 4b. The shape factor was calculated
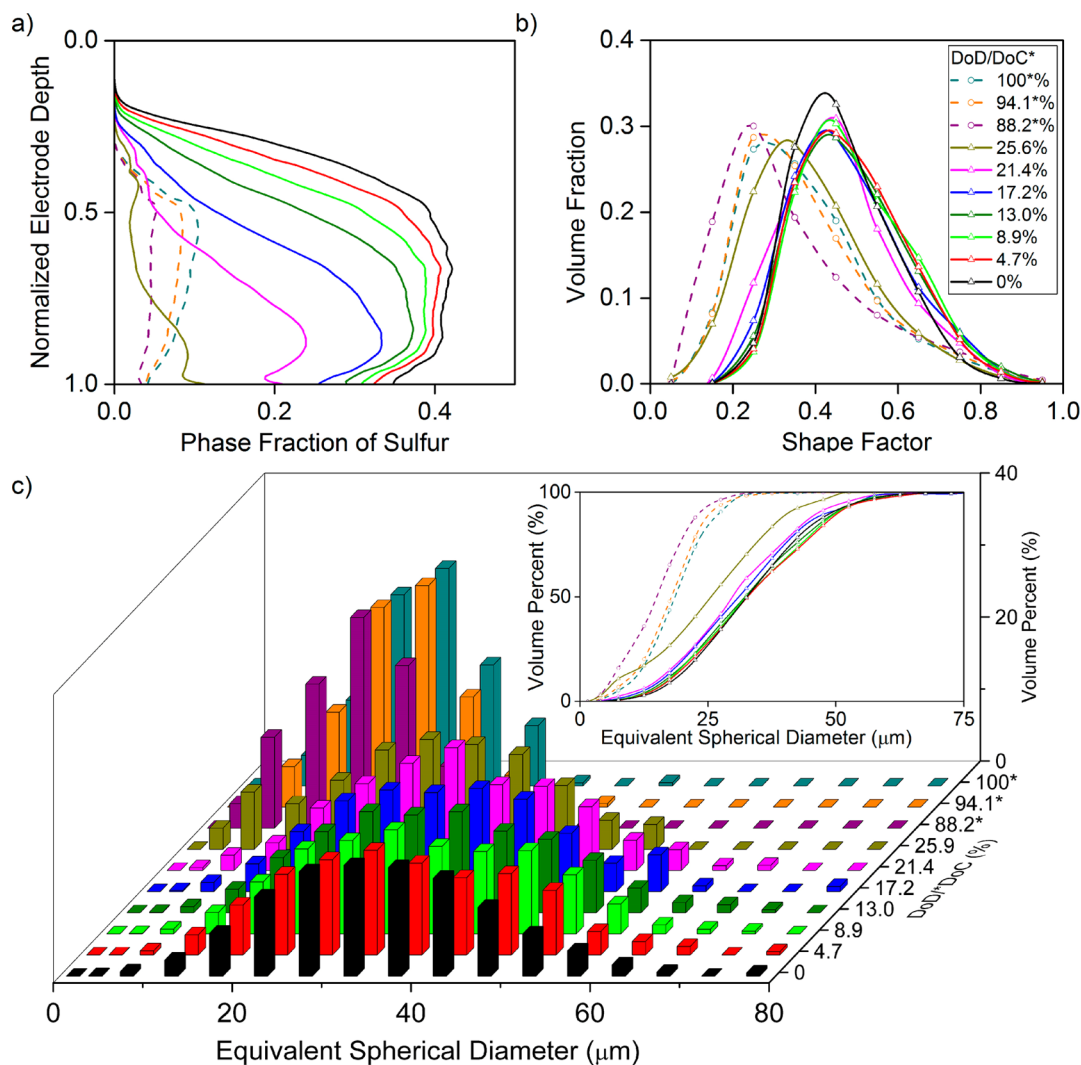
Figure 4. (a) Phase fraction as a function of electrode thickness normalized to (0,1) between fixed positions in the separator and current collector respectively, (b) shape factor distribution of sulfur particles during discharge and charge, and (c) particle size distributions with cumulative distributions inset. Legend in (b) applies to all plots. Asterisk indicates depth of charge values.

through the method described by Haibel et al.[28] There is a marked shift of the PSD between the uncycled cell (at 0% DoD) and the charged cell (at 100% DoC after the first cycle), with the mean equivalent spherical diameter decreasing from ca. 34.8 μm with a D50 of ca. 41 μm to ca. 21.0 μm with a D50 of ca. 18.5 μm, respectively. The D50, or particle size at 50% of the cumulative size distribution, is a commonly used parameter to describe particle systems. In addition, the particle shape factor distribution shifts toward smaller values upon charge, indicative of less spherical particles, which would be characteristic of S_8 in its monoclinic form (β-S_8).

To demonstrate the advantages of volumetric data in resolving individual particles within electrodes, maximum intensity projections were performed on tomograms of the sulfur electrode in the through-plane direction. The resulting projections (Figure 5a,b, left), represent an approximation to the radiographs obtained in transmission X-ray microscopy (TXM). While valuable insights may be gained from TXM experiments that offer a higher temporal resolution, the 2D nature of this technique means that there is often a need for dilute electrodes, or in the case of Li−S battery chemistry,

polysulfide cells. These additional factors introduce some uncertainty in the conclusions drawn from these experiments.

The comparisons presented in Figure 5a,b highlight the unique capabilities of X-ray micro-CT on imaging fully functioning and representative electrodes; the loss of one spatial dimension diminishes the ability to resolve individual features within the electrodes. For instance, Risse et al.[12] observed the formation of needle-like structures using TXM during charging of a polysulfide cell, hypothesized to be macroscopic crystals of metastable β-S_8. As demonstrated in Figure 5b, volumetric data of the sulfur electrode at a spatial resolution of approximately an order of magnitude greater revealed that these macroscopic crystals were, in fact, composed of many smaller individual crystallites of sulfur embedded within the CBD as shown in Figure 3g−i. The volumetric image data also reveals that the spatial distribution of sulfur formation during charge may be influenced by the anisotropic growth of β-S_8 crystallites, first proposed by Kulisch et al. based on intensity variations in the characteristic X-ray diffraction peaks,[15] extending macroscopically throughout the sulfur electrode.
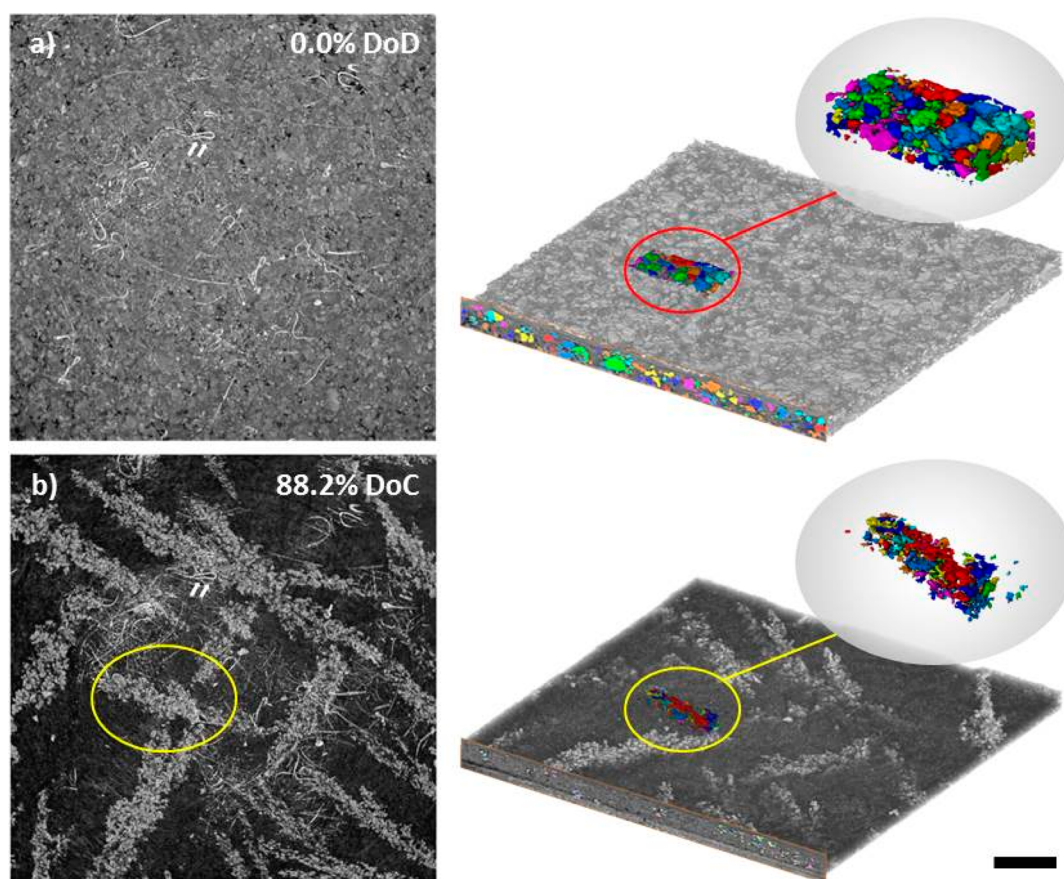
Figure 5. Maximum intensity projections of sulfur electrode at (a) uncycled state, and (b) first appearance of sulfur at 88.2% depth of charge. White arrows indicate landmark present in both projections, yellow circle indicates the needle-like projections formed during charge, and red circle shows the same volume in the uncycled cell. Scale bar represents 100 μm for the magnified volume renderings and 200 μm for all other images.

Contrast Analysis of the Carbon Binder Domain and Bulk Pore Phase. A potential challenge in imaging Li−S cells with micro-CT is capturing the reactions involving polysulfide species dissolved in the liquid electrolyte, as phase identification can be difficult due to the lack of well-defined particles and structures. Furthermore, it is challenging to resolve Li$_2$S with the ca. 0.81 μm voxel size of the tomograms utilized here, and various authors have shown through XRD[9,10,15] and TXM[12] studies that no macroscopic Li$_2$S crystals are formed. The intensity of a voxel containing more than one phase is proportional to the averaged linear attenuation coefficients of its constituent phases and is therefore linked to the nanoscopic features present within the porous CBD and Li$_2$S.

As seen in Figure 6a, there is initially a small difference in contrast between the CBD phase and bulk pore phase as the highly porous CBD phase is, in itself, percolated with the electrolyte present in the bulk pore phase. Fortunately, as evident in the progression from Figure 6a−e, it gradually becomes possible to distinguish a brighter CBD phase from a darker bulk pore phase at higher depths of discharge. It is hypothesized that this is due to a combination of factors: the formation of denser Li$_2$S within the porous network of the CBD as well as a reduction in the density of the electrolyte associated with a depletion of polysulfide species as discharge progresses. No significant changes to the microstructure of the CBD are detectable at this resolution as a result of Li$_2$S formation, despite notable changes in the attenuation contrast. The presence of the CBD provides a structure that can be segmented from the bulk electrolyte-filled pore phase, and changes in the intensities of the CBD phase and the bulk pore phase can therefore be decoupled.

While some generalized conclusions can be drawn about Li$_2$S formation and changes in electrolyte density from the histogram analysis, definitive phase quantification of Li$_2$S is not possible without deconvolution of the density contribution from the electrolyte within the porous CBD. Density changes within the electrolyte phase are significant as the concentration of polysulfide species fluctuate depending on state of charge. Peaks in the normalized intensity of the bulk pore phase were reached at point (a) and slightly before point (i) in Figure 6, corresponding to the point of complete sulfur disappearance during discharge and immediately preceding the recrystallization of sulfur during charge, respectively. This suggests that the electrolyte was at its most saturated state when the concentration of higher order polysulfide species in solution was highest. Between points (a) and (b) there was a decrease in normalized intensities in both the bulk pore and porous CBD phases, and it is hypothesized that this is due to an increase in the lithium content of the dissolved polysulfide species reducing the density of the electrolyte in both phases. The intensity of the bulk pore phase then trends downward as discharge progresses, with a concomitant *increase* in intensity of the CBD phase as polysulfide species precipitate out solution to form Li$_2$S in the CBD.

During charge, the reverse takes place where electrolyte density increases and the density of the CBD phase decreases
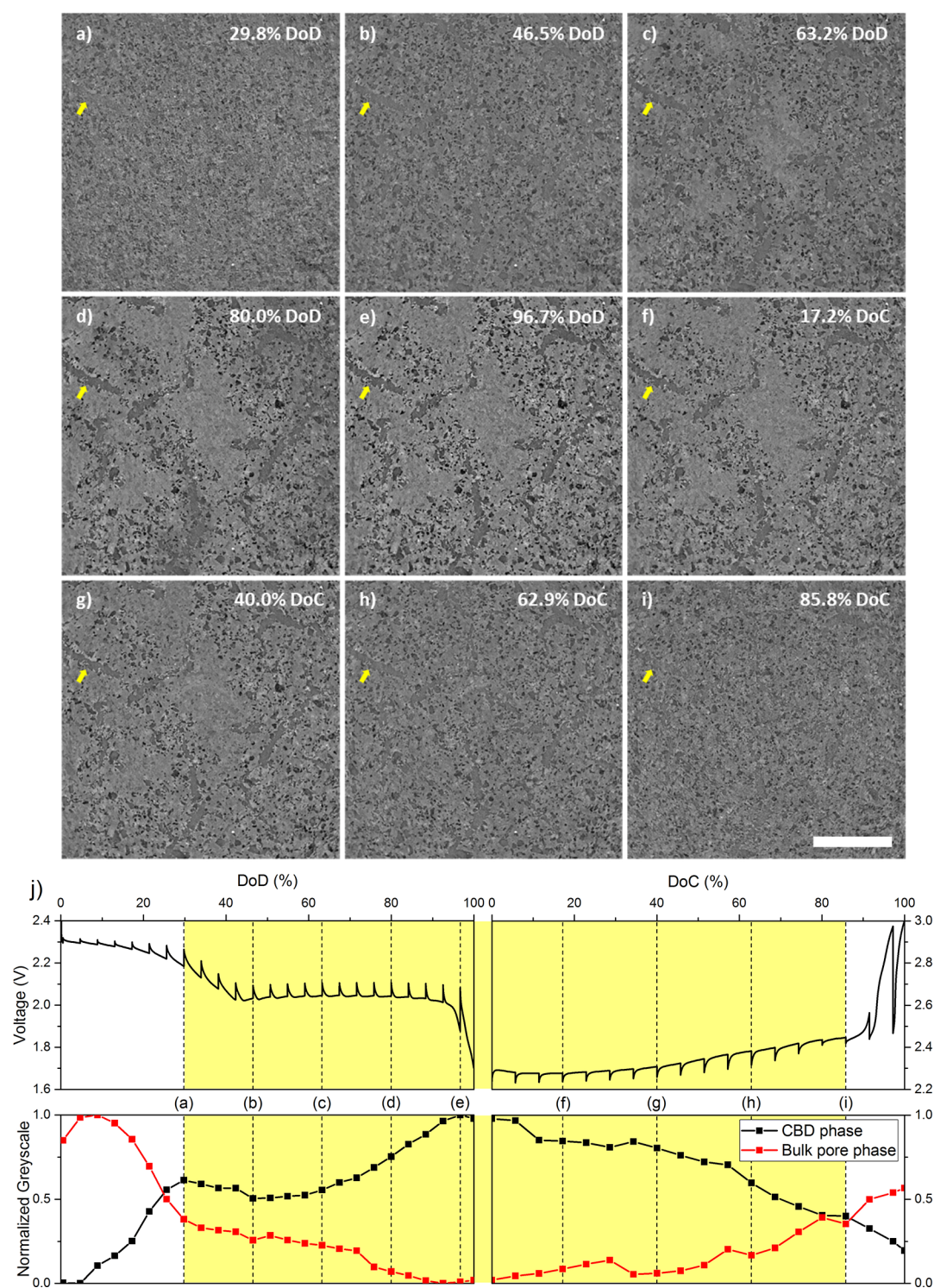
Figure 6. (a−e) Cross-sectional virtual slices of the sulfur electrode taken at the same electrode height at various depths of discharge and (f−i) charge where elemental sulfur was not visible. Normalized mean histogram values for the CBD phase and bulk pore phase as a function of state of charge. (j) Voltage profiles (top) and normalized mean histogram values (bottom) for the CBD phase and bulk pore phase as a function of state of charge. Scale bar represents 400 μm.

as Li_2S dissolves to form lower order polysulfide species that are progressively oxidized to denser higher order polysulfide species with a loss of lithium content. At the end of the first cycle, the normalized grayscale of the CBD phase falls below its original value. Along with a significantly darker phase becoming noticeable in Figure 6e−i and dips in the mean contrast values of the bulk pore phase, it is hypothesized that

bubble formation may have taken place, although further investigation may be required to confirm this effect.

■ CONCLUSIONS

The direct visualization of a Li−S cell with X-ray micro-CT has provided unprecedented insight into its microstructural evolution as a function of state of charge, with definitive

quantification of the solid sulfur phase within the cathode. To the authors' knowledge, this is the first time that the carbon and binder domain has been successfully resolved in an in situ cell. While the CBD was found to remain relatively unchanged despite large volume changes within the cell in the initial cycle, further investigation is required to determine the extent that the cyclic growth and dissolution of sulfur influences microstructural degradation in the CBD. Future work of value will focus on longitudinal studies of cell and electrode aging over extended cycling. Despite some limitations of micro-CT in identifying soluble polysulfide species and nanosized Li_2S, no characterization technique is uniquely suited to fully explain the highly complex multiphase phenomena underpinning Li−S battery chemistry.[8] Multimodal tomographic configurations involving two or more techniques will be able to provide a more complete picture of the mechanisms with the Li−S cell. For instance, the combination of phase contrast micro-CT with micron-scale X-ray diffraction computed tomography (XRD-CT) will provide complementary information about the crystalline states of sulfur and lithium sulfide.

The value of 4D investigations extends beyond enhancing the mechanistic understanding of nascent electrochemical technologies and the identification of degradation pathways and failure modes. Volumetric image data can serve as a starting point for true 3D electrochemical modeling of batteries. This is particularly relevant for conversion-type chemistries, such as Li−S batteries, where well-established continuum models may fail to encapsulate the large and potentially anisotropic changes that occur.

■ METHODS

Electrode Preparation and Cell Fabrication. Elemental sulfur (325 mesh, Alfa Aesar), conductive carbon black (Super C65, Timcal), Ketjenblack (EC600-JD, Akzo Nobel), and polyvinylidene fluoride binder (Solef 5130, Solvay) in a 75:12:3:10 weight ratio were homogenized in N-methyl-2-pyrrolidinone (NMP, Sigma-Aldrich) by a high shear laboratory mixer (L5M, Silverson) to form an ink with 20% total solids content. The ink was cast onto 15 μm thick aluminum foil (MTI Corp.) using a micrometer adjustable film applicator set to a blade gap of 400 μm.

The Li−S cells were assembled in modified 1/8″ PFA Swagelok straight unions (PFA-220-6, Swagelok), with the sulfur electrode laser-cut to 3 mm diameter as the positive electrode, glass fiber (Whatman GF/D) between two layers of polyolefin membrane (Celgard 2400) as the separator, and Li foil punched to 1/8″ diameter as the negative electrode. Stainless steel plungers provided compression, as well as electrical connection, to the electrodes, and the electrolyte used was 1 M lithium bis(trifluoromethane) sulfonimide (LiTFSI) in 1,3-dioxolane and 1,2-dimethoxyethane (DOL/DME, 1:1 v/v) with 0.3 M lithium nitrate as additive (Soulbrain, MI). All the cells were assembled in an argon-filled glovebox (LABstar, MBraun) with oxygen and moisture levels kept at <0.5 ppm and transported to the synchrotron facility over 3 Å molecular sieves in argon-filled containers. Although each cell was initially filled with 20 μL of electrolyte from a micropipette (Eppendorf Research plus, Eppendorf AG), excess electrolyte was squeezed out by compression during final assembly, and the final E/S ratio within the electrode stack was estimated to be less than 2 mL g^{-1} or less than 5 mL g^{-1} including dead volume within the cell of ca. 2 μL.

X-ray Microtomography and Reconstruction. In situ experiments were conducted at the I13-2 Diamond-Manchester branchline of the I13 imaging beamline at Diamond Light Source, with a ca. 22 keV X-ray beam monochromatized by a multilayer monochromator (MLM) vanadium stripe. A 500 μm CdWO$_4$ scintillator was coupled

to a 4× objective lens mounted onto a PCO.edge5.5 CCD camera for 8× total optical magnification, resulting in an isotropic pixel size of ca. 0.81 μm and field of view of ca. 2.1 × 1.8 mm. The sample to detector distance was set to ca. 135 mm to enhance propagation-based in-line phase contrast as described by Mayo et al.[29] The cell was rotated in small angular increments over 180° for a total of 1501 radiographs captured with an exposure time of 0.75 s per frame, resulting in a ca. 15 min acquisition rate for each tomogram. During each tomographic acquisition, the cell was held at open circuit voltage to ensure a consistent state of charge throughout the scan. The radiographic acquisitions were reconstructed using a parallel beam filtered back-projection algorithm[30] to produce tomograms with dimensions of 2568 × 2560 × 650 cubic voxels, containing the entire height of the Li−S cell.

Electrochemical Cycling. The cell was electrochemically cycled with a potentiostat (Interface 1000E, Gamry Instruments) at an effective C/5 rate split into 15 min intervals (i.e., 5 h for the first discharge) while mounted on the sample stage. The beam shutter was closed during each electrochemical cycling step to minimize the effects of beam damage to the cell.

Image Postprocessing, Segmentation, and Analysis. The tomograms were imported into Avizo (Thermo Fisher Scientific) and MATLAB (MathWorks, Inc.) for postprocessing, segmentation, and image analysis. For visualization and segmentation purposes, a combination of edge-preserving smoothing 3D bilateral and nonlocal means filters were used to reduce noise within the image. Cropped subvolumes of each tomogram, with dimensions of 1810 × 1815 × 139 cubic voxels, containing the entire sulfur cathode were extracted, and the Avizo Auto Threshold module based on Otsu's method[31] was used to perform an approximate segmentation of the cathode into sulfur and nonsulfur phases. The approximate segmentation served as a seed for a marker-based watershed segmentation to correct for partial volume effects and phase boundaries between high and low intensities.[32] Individual particles in the label fields of the watershed segmentation output were separated and identified in Avizo, and particle size distributions were calculated, excluding particles smaller than 50 cubic voxels.

In order to calculate the mass loading of the entire cathode for tomograms where elemental sulfur was detected, the sulfur dissolution front was determined by radially integrating the original tomograms from the central axis of the electrode using the Radial Profile ImageJ plugin. This was possible because the tomograms at 21.4 and 25.6% DoD had a circular dissolution front fully within the field of view, with negligible amounts of sulfur detected beyond the dissolution front. For tomograms at lower DoDs, a smaller radial integration angle was used as only part of the dissolution front was within the field of view. A series of 2D radial profiles were obtained from the tomograms and are presented in the Supporting Information. The sulfur mass loading was then calculated by normalizing the mass of sulfur within the dissolution front across the known electrode diameter.

Maximum intensity images of the cropped tomograms described earlier were projected in Avizo in the direction orthogonal to the current collector by taking the intensity maxima, resulting in 2D images approximating transmission X-ray microscopy.

Histogram analysis on each phase was performed in MATLAB on the raw 3D data masked to contain only the phases of interest. Given the relatively limited volume expansion of the CBD, a mask of the CBD phase was segmented from the tomogram at the end of discharge when the contrast was greatest and used to quantify volume-averaged contrast changes within the CBD phase and bulk pore phase throughout all data sets. Because of the region of interest nature of the tomographies that were carried out, only data sets without the significantly more attenuating and distinct sulfur phase were considered for this analysis to reduce the artifacts associated with material outside the FOV. However, mean grayscale values were calculated from all data sets for completeness, with corresponding cross-sectional virtual slices available as a movie in Supporting Information. The contrast of each tomogram was matched by histogram equalization based on the same subvolume deep within the bulk Li phase that remained constant during cycling. The histograms

of each phase approximated Gaussian distributions, and the mean values presented in Figure 6 correspond to the peak of the distribution curves normalized to between 0 and 1.

■ ASSOCIATED CONTENT

Ⓢ Supporting Information

The Supporting Information is available free of charge on the ACS Publications website at DOI: 10.1021/acsaem.8b01148.

Supporting figure for radial correction factor (PDF)
Supporting movie for histogram analysis (AVI)

■ AUTHOR INFORMATION

Corresponding Author
*E-mail: p.shearing@ucl.ac.uk.
ORCID Ⓞ
Paul R. Shearing: 0000-0002-1387-9531
Notes
The authors declare no competing financial interest.

■ ACKNOWLEDGMENTS

■ REFERENCES

(1) Bruce, P. G.; Freunberger, S. A.; Hardwick, L. J.; Tarascon, J. M. Li-O2 and Li-S Batteries with High Energy Storage. *Nat. Mater.* **2012**, *11*, 19−29.

(2) Nazar, L. F.; Cuisinier, M.; Pang, Q. Lithium-Sulfur Batteries. *MRS Bull.* **2014**, *39*, 436−442.

(3) Jozwiuk, A.; Berkes, B. B.; Weiß, T.; Sommer, H.; Janek, J.; Brezesinski, T. The Critical Role of Lithium Nitrate in the Gas Evolution of Lithium−Sulfur Batteries. *Energy Environ. Sci.* **2016**, *9*, 2603−2608.

(4) Ji, X.; Lee, K. T.; Nazar, L. F. A Highly Ordered Nanostructured Carbon-Sulphur Cathode for Lithium-Sulphur Batteries. *Nat. Mater.* **2009**, *8*, 500−6.

(5) Pope, M. A.; Aksay, I. A. Structural Design of Cathodes for Li-S Batteries. *Adv. Energy Mater.* **2015**, *5*, 1500124.

(6) Ogoke, O.; Wang, X.; Casimir, A.; Ma, L.; Wu, T.; Wu, G.; Lu, J. Effective Strategies for Stabilizing Sulfur for Advanced Lithium-Sulfur Batteries. *J. Mater. Chem. A* **2017**, *5*, 448−469.

(7) Tan, J.; Liu, D.; Xu, X.; Mai, L. In Situ/Operando Characterization Techniques for Rechargeable Lithium-Sulfur Batteries: A Review. *Nanoscale* **2017**, *9*, 19001−19016.

(8) Conder, J.; Villevieille, C. Is the Li−S Battery an Everlasting Challenge for Operando Techniques? *Current Opinion in Electrochemistry* **2018**, *9*, 33−40.

(9) Cañas, N. A.; Wolf, S.; Wagner, N.; Friedrich, K. A. In-Situ X-Ray Diffraction Studies of Lithium−Sulfur Batteries. *J. Power Sources* **2013**, *226*, 313−319.

(10) Walus, S.; Barchasz, C.; Colin, J. F.; Martin, J. F.; Elkaim, E.; Lepretre, J. C.; Alloin, F. New Insight into the Working Mechanism of Lithium-Sulfur Batteries: In Situ and Operando X-Ray Diffraction Characterization. *Chem. Commun. (Cambridge, U. K.)* **2013**, *49*, 7899−901.

(11) Yu, S.-H.; Huang, X.; Schwarz, K.; Huang, R.; Arias, T.; Brock, J.; Abruna, H. D. Direct Visualization of Sulfur Cathodes: New Insights into Li-S Batteries Via Operando X-Ray Based Methods. *Energy Environ. Sci.* **2018**, *11*, 202.

(12) Risse, S.; Jafta, C. J.; Yang, Y.; Kardjilov, N.; Hilger, A.; Manke, I.; Ballauff, M. Multidimensional Operando Analysis of Macroscopic Structure Evolution in Lithium Sulfur Cells by X-Ray Radiography. *Phys. Chem. Chem. Phys.* **2016**, *18*, 10630−6.

(13) Yang, Y.; Risse, S.; Mei, S.; Jafta, C. J.; Lu, Y.; Stöcklein, C.; Kardjilov, N.; Manke, I.; Gong, J.; Kochovski, Z.; Ballauff, M. Binder-Free Carbon Monolith Cathode Material for Operando Investigation of High Performance Lithium-Sulfur Batteries with X-Ray Radiography. *Energy Storage Materials* **2017**, *9*, 96−104.

(14) Nelson, J.; Misra, S.; Yang, Y.; Jackson, A.; Liu, Y.; Wang, H.; Dai, H.; Andrews, J. C.; Cui, Y.; Toney, M. F. Operando X-Ray Diffraction and Transmission X-Ray Microscopy of Lithium Sulfur Batteries. *J. Am. Chem. Soc.* **2012**, *134*, 6337−43.

(15) Kulisch, J.; Sommer, H.; Brezesinski, T.; Janek, J. Simple Cathode Design for Li-S Batteries: Cell Performance and Mechanistic Insights by in Operando X-Ray Diffraction. *Phys. Chem. Chem. Phys.* **2014**, *16*, 18765−71.

(16) Zielke, L.; Barchasz, C.; Walus, S.; Alloin, F.; Lepretre, J. C.; Spettl, A.; Schmidt, V.; Hilger, A.; Manke, I.; Banhart, J.; et al. Degradation of Li/S Battery Electrodes on 3d Current Collectors Studied Using X-Ray Phase Contrast Tomography. *Sci. Rep.* **2015**, *5*, 10921.

(17) Sun, F.; Osenberg, M.; Dong, K.; Zhou, D.; Hilger, A.; Jafta, C. J.; Risse, S.; Lu, Y.; Markötter, H.; Manke, I. Correlating Morphological Evolution of Li Electrodes with Degrading Electrochemical Performance of Li/Licoo2 and Li/S Battery Systems: Investigated by Synchrotron X-Ray Phase Contrast Tomography. *ACS Energy Letters* **2018**, *3*, 356−365.

(18) Wolf, M.; May, B. M.; Cabana, J. Visualization of Electrochemical Reactions in Battery Materials with X-Ray Microscopy and Mapping. *Chem. Mater.* **2017**, *29*, 3347−3362.

(19) Heenan, T. M. M.; Finegan, D. P.; Tjaden, B.; Lu, X.; Iacoviello, F.; Millichamp, J.; Brett, D. J. L.; Shearing, P. R. 4d Nano-Tomography of Electrochemical Energy Devices Using Lab-Based X-Ray Imaging. *Nano Energy* **2018**, *47*, 556−565.

(20) Yermukhambetova, A.; Tan, C.; Daemi, S. R.; Bakenov, Z.; Darr, J. A.; Brett, D. J.; Shearing, P. R. Exploring 3d Microstructural Evolution in Li-Sulfur Battery Electrodes Using in-Situ X-Ray Tomography. *Sci. Rep.* **2016**, *6*, 35291.

(21) Tan, C.; Randjbar Daemi, S.; Brett, D. J.; Shearing, P. Investigating the Three-Dimensional Microstructural Characteristics of Lithium-Sulfur Electrodes with X-Ray Micro-Tomography. *ECS Trans.* **2017**, *77*, 447.

(22) Tonin, G.; Vaughan, G.; Bouchet, R.; Alloin, F.; Di Michiel, M.; Boutafa, L.; Colin, J. F.; Barchasz, C. Multiscale Characterization of a Lithium/Sulfur Battery by Coupling Operando X-Ray Tomography and Spatially-Resolved Diffraction. *Sci. Rep.* **2017**, *7*, 2755.

(23) Barghamadi, M.; Best, A. S.; Bhatt, A. I.; Hollenkamp, A. F.; Musameh, M.; Rees, R. J.; Rüther, T. Lithium−Sulfur Batteries—the Solution Is in the Electrolyte, but Is the Electrolyte a Solution? *Energy Environ. Sci.* **2014**, *7*, 3902−3920.

(24) Nelson, J.; Yang, Y.; Misra, S.; Andrews, J. C.; Cui, Y.; Toney, M. F. Identifying and Managing Radiation Damage During in Situ Transmission X-Ray Microscopy of Li-Ion Batteries. *Proc. SPIE* **2013**, *8851*, 88510B.

(25) Wild, M.; O'Neill, L.; Zhang, T.; Purkayastha, R.; Minton, G.; Marinescu, M.; Offer, G. J. Lithium Sulfur Batteries, a Mechanistic Review. *Energy Environ. Sci.* **2015**, *8*, 3477−3494.

(26) Barchasz, C.; Molton, F.; Duboc, C.; Lepretre, J. C.; Patoux, S.; Alloin, F. Lithium/Sulfur Cell Discharge Mechanism: An Original Approach for Intermediate Species Identification. *Anal. Chem.* **2012**, *84*, 3973−80.

(27) Xu, R.; Lu, J.; Amine, K. Progress in Mechanistic Understanding and Characterization Techniques of Li-S Batteries. *Adv. Energy Mater.* **2015**, *5*, 1500408.

(28) Haibel, A.; Manke, I.; Melzer, A.; Banhart, J. In Situ Microtomographic Monitoring of Discharging Processes in Alkaline Cells. *J. Electrochem. Soc.* **2010**, *157*, A387.

(29) Mayo, S. C.; Stevenson, A. W.; Wilkins, S. W. In-Line Phase-Contrast X-Ray Imaging and Tomography for Materials Science. *Materials* **2012**, *5*, 937−965.

(30) Kak, A. C.; Slaney, M. *Principles of Computerized Tomographic Imaging*; IEEE Press, 1988.

(31) Otsu, N. A Threshold Selection Method from Gray-Level Histograms. *IEEE Transactions on Systems, Man, and Cybernetics* **1979**, *9*, 62−66.

(32) Landis, E. N.; Keane, D. T. X-Ray Microtomography. *Mater. Charact.* **2010**, *61*, 1305−1316.